

Disorder from order among anisotropic next-nearest-neighbor Ising spin chains in SrHo_2O_4

J.-J. Wen,^{1,*} W. Tian,² V. O. Garlea,² S. M. Koohpayeh,¹ T. M. McQueen,^{1,3} H.-F. Li,^{4,5} J.-Q. Yan,⁶ J. A. Rodriguez-Rivera,^{7,8} D. Vaknin,⁹ and C. L. Broholm^{1,2,7}

¹*Institute for Quantum Matter and Department of Physics and Astronomy,
The Johns Hopkins University, Baltimore, Maryland 21218, USA*

²*Quantum Condensed Matter Division, Oak Ridge National Laboratory, Oak Ridge, Tennessee 37831, USA*

³*Department of Chemistry and Department of Materials Science and Engineering,
The Johns Hopkins University, Baltimore, Maryland 21218, USA*

⁴*Jülich Centre for Neutron Science JCNS, Forschungszentrum Jülich GmbH,
Outstation at Institut Laue-Langevin, Boîte Postale 156, F-38042 Grenoble Cedex 9, France*

⁵*Institut für Kristallographie der RWTH Aachen University, D-52056 Aachen, Germany*

⁶*Department of Materials Science and Engineering,
The University of Tennessee, Knoxville, Tennessee 37996, USA*

⁷*NIST Center for Neutron Research, National Institute of Standards and Technology, Gaithersburg, Maryland 20899, USA*

⁸*Department of Materials Science and Engineering,
University of Maryland, College Park, Maryland 20742, USA*

⁹*Ames Laboratory and Department of Physics and Astronomy, Iowa State University, Ames, Iowa 50011, USA*

(Dated: September 30, 2018)

We describe why Ising spin chains with competing interactions in SrHo_2O_4 segregate into ordered and disordered ensembles at low temperatures (T). Using elastic neutron scattering, magnetization, and specific heat measurements, the two distinct spin chains are inferred to have Néel ($\uparrow\downarrow\uparrow\downarrow$) and double-Néel ($\uparrow\uparrow\downarrow\downarrow$) ground states respectively. Below $T_N = 0.68(2)$ K, the Néel chains develop three dimensional (3D) long range order (LRO), which arrests further thermal equilibration of the double-Néel chains so they remain in a disordered incommensurate state for T below $T_S = 0.52(2)$ K. SrHo_2O_4 distills an important feature of incommensurate low dimensional magnetism: kinetically trapped topological defects in a quasi- d -dimensional spin system can preclude order in $d + 1$ dimensions.

I. INTRODUCTION

An interesting byproduct of the intense pursuit of materials that can host spin-liquids has been the discovery of nominally pure crystalline solids with frozen short range correlated magnetism.^{1–5} In some cases quenched disorder simply alters the ground state and defines a short spin correlation length, but for materials such as two dimensional SCGO⁶ and NiGa_2S_4 ⁴ where the spin correlation length is much shorter than a plausible impurity spacing such explanations seem untenable. Instead in the present study, we propose that spin disorder in frustrated low dimensional magnets can result from a complex thermalization process in the absence of quenched disorder.

Comprising two types of Ising spin chains with nearest neighbor (J_1) and next nearest neighbor (J_2) interactions [anisotropic next-nearest-neighbor (ANNNI) models⁷] organized on a honeycomb-like lattice, SrHo_2O_4 provides a striking example.^{8–13} We show the chains straddle the $J_2/J_1 = 1/2$ critical point so that “red” chains have a ground state that doubles the unit cell ($\uparrow\downarrow\uparrow\downarrow$) while the ground state for “blue” chains is a double-Néel state ($\uparrow\uparrow\downarrow\downarrow$) [as illustrated in Fig. 1(b)]. While red chains develop 3D LRO, blue chains in the very same crystal cease further equilibration towards their more complex ground state when the red spins saturate in an ordered state.

SrHo_2O_4 belongs to a family of iso-structural rare-earth strontium oxides, SrRE_2O_4 .^{8–18} Recent experi-

ments on this series of materials have revealed low temperature magnetic states ranging from a disordered state in SrDy_2O_4 ¹³ to noncollinear 3D LRO in SrYb_2O_4 ¹⁶. A very unusual coexistence of a 3D LRO and 1D short range order (SRO) was discovered in polycrystalline and single crystalline samples of SrHo_2O_4 ^{11–13} and SrEr_2O_4 ^{14,15}. No explanation for the coexistence of two drastically different types of correlations over different length scales in the same crystal has so far been provided. With the additional experimental results and analysis presented here, we are able to provide an explanation for a partially ordered magnetic state where quenched disorder does not play an essential role.

II. EXPERIMENTAL METHODS

A. Crystal structure and synthesis

SrHo_2O_4 crystallizes in space group $Pnam$ ⁸ with two inequivalent Ho sites [Fig. 1(a)]. Both are Wyckoff 4c sites with mirror planes perpendicular to the \mathbf{c} direction where Ho is surrounded by 6 oxygen atoms forming a distorted octahedron. The magnetic lattice consists of zig-zag ladders which extend along \mathbf{c} and form a honeycomb-like pattern in the $\mathbf{a} - \mathbf{b}$ plane [Fig. 1(b)].

Polycrystalline powders of SrHo_2O_4 were prepared by solid state synthesis using Ho_2O_3 (99.99 %) and SrCO_3

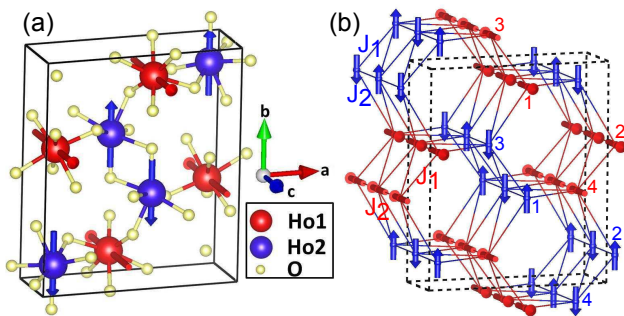


FIG. 1. (a) Crystallographic unit cell of SrHo_2O_4 . Sr atoms were omitted for clarity. Red and Blue spheres show two distinct Ho sites, and the corresponding arrows show the Ising spin directions. (b) Magnetic lattice formed by Ho and a schematic representation of the spin structure determined by neutron diffraction.

(99.99%) as starting materials. The starting powders were mixed, pressed into pellets, and heated at 900, 1000 and 1100 °C in air, each for 10 h with intermediate grinding. 4% extra SrCO_3 was added to the starting materials to account for evaporation of Sr during single crystal growth. After grinding and phase identification, synthesized powders were compacted into a rod using a hydraulic press. The feed rods were then sintered at 1200 °C for 10 h in air. Single crystals with diameter 4-5 mm and length up to 60 mm were grown from the polycrystalline feed rods in a four-mirror optical floating zone furnace (Crystal Systems Inc. FZ-T-12000-X-VPO-PC) with 4×3 kW xenon lamps. The growth rate was 4 mm/h with rotation rates of 5 rpm for the growing crystal (lower shaft) and 0 rpm for the feed rod (upper shaft) in a 4 bar purified argon atmosphere. Growth under oxygen containing atmospheres led to significant evaporation of phases containing Sr, and Ho_2O_3 was formed as second phase inclusions in the as grown crystals.

B. Thermomagnetic and neutron scattering measurements

The thermomagnetic properties of SrHo_2O_4 were measured using a Physical Properties Measurement System from Quantum Design, Inc. with a dilution refrigerator option for measurements below 1.8 K. Heat capacity measurements were performed using the quasi-adiabatic heat-pulse technique on a thin plate of polished single crystalline SrHo_2O_4 . Temperature dependent magnetization measurements between 2 K and 300 K along three crystalline axes were carried out using a vibrating sample magnetometer option in a magnetic field of 200 Oe.

Elastic neutron scattering (ENS) maps for T down to 1.5 K were measured on MACS¹⁹ at the NIST Center for Neutron Research with $E_i = E_f = 5$ meV neutrons. A 4.3 g single crystal was mounted for consecutive experiments in the $(HK0)$ and $(0KL)$ planes. Single crys-

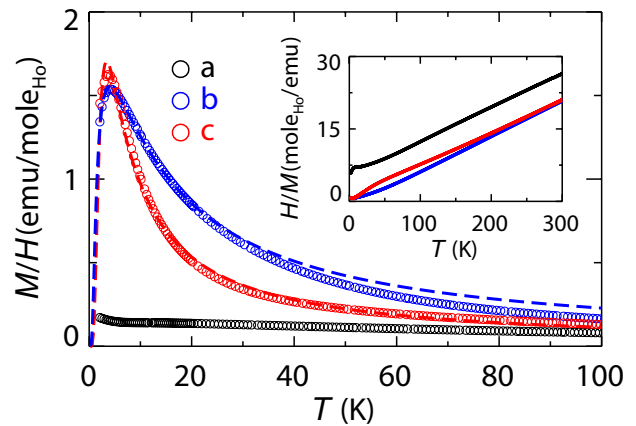


FIG. 2. Magnetic susceptibility of SrHo_2O_4 along three axes measured under 200 Oe. Dashed lines show fits to $J_1 - J_2$ Ising models. The inset shows the inverse magnetic susceptibility up to 300 K.

tal ENS measurement for T down to 0.28 K in a ^3He insert were conducted on the HB-1A instrument at the High Flux Isotope Reactor of ORNL. Samples cut to the shape of small cubes with masses of 0.34 g and 0.19 g to reduce the effects of neutron absorption were used for measurements in the $(0KL)$ and (HOL) planes respectively. The sample mount was made from oxygen-free copper to ensure good thermal contact at low T . Temperature dependent measurements were carried out upon warming after cooling to the 0.28 K base temperature of the pumped ^3He system.

III. EXPERIMENTAL RESULTS

A. Thermomagnetic measurements

The magnetic susceptibility χ of SrHo_2O_4 , approximated by M/H with a measuring field of $H = 200$ Oe, is shown in Fig. 2. χ_a is found to be an order of magnitude smaller than χ_b and χ_c , indicating strong magnetic anisotropy with a hard axis along **a**. χ_b and χ_c increase upon cooling and form broad peaks for $T \sim 5$ K that are characteristic of antiferromagnetic (AFM) SRO.⁸⁻¹⁰ The inset in Fig. 2 shows the inverse magnetic susceptibility χ^{-1} for T between 2 K and 300 K. A Curie-Weiss analysis of the approximately linear regime between 100 K and 300 K results in effective moment sizes P_{eff} of $10.1(1) \mu_B$, $10.5(1) \mu_B$, and $11.8(1) \mu_B$, and Weiss temperature Θ_{CW} of $-63.5(3)$ K, $16.4(1)$ K, and $-27.6(2)$ K for the **a**, **b**, and **c** directions respectively. These P_{eff} values are consistent with an 5I_8 electronic configuration for $4f^{10} \text{Ho}^{3+}$. While Θ_{CW} is usually associated with inter-spin interactions, such an interpretation is not straight forward here since the high temperature χ is also affected by the crystalline electric field (CEF)²⁰ level scheme for Ho^{3+} in SrHo_2O_4 .

The temperature dependent specific heat of SrHo_2O_4 is shown in Fig. 3(a). Filled symbols show the experimental specific heat C_{total} . The broad peak for $T \sim 5$ K corresponds to SRO also indicated by a maximum in χ . A second anomaly is observed at $T \sim 0.2$ K. There is a single stable isotope of holmium, ^{165}Ho with a finite nuclear spin $I = 7/2$, the multiplet of which can be split through hyperfine interactions with electronic spins. This produces a peak in the specific heat at low temperatures, the so called nuclear Schottky anomaly (C_{nuc}).²¹ By assuming a $7.7(2) \mu_{\text{B}}$ static magnetic moment for electronic spins of Ho^{3+} , the low temperature C_{total} peak can be very well accounted for by the nuclear Schottky anomaly, as shown by the magenta long dashed line in Fig. 3(a). After subtracting C_{nuc} from C_{total} , the contribution to specific heat from electronic spins (C_{mag}) is obtained and shown as open symbols in Fig. 3(a). The phonon contribution to the specific heat is negligible in the temperature range probed.

A kink in C_{mag} is observed at $T_{\text{N}} = 0.61(2)$ K, which is even more apparent as a sharp peak in C_{mag}/T indicating a bulk phase transition [Fig. 3(b)]. The magnetic entropy (S) inferred from the area under the C_{mag}/T curve is shown in Fig. 3(c).

B. Neutron scattering

For a direct view of the short range spin correlations indicated by the thermodynamic anomalies for $T \sim 5$ K, Fig. 4(a)-(d) show ENS intensity maps covering the $(HK0)$ and $(0KL)$ planes. The strongly anisotropic nature of the wave vector dependence indicates quasi-1D correlations along the \mathbf{c} -axis consistent with previous data.^{9,12} The modulation in the $(HK0)$ plane takes the form of a checker-board-like structure [Fig. 4(a) and (c)] and is associated with intra-ladder correlations. The fact that this scattering occurs for $\mathbf{q}_{\mathbf{c}} = 0$ but vanishes near $\mathbf{q} = 0$ indicates an AFM structure that is not modulated along \mathbf{c} . The $(0KL)$ intensity map reveals another type of correlations with $\mathbf{q}_{\mathbf{c}} \sim 0.5\mathbf{c}^*$, where $\mathbf{c}^* \equiv \frac{2\pi}{c}$. The intensity maximum near $\mathbf{q}_{\mathbf{c}} \sim 0.5\mathbf{c}^*$ indicates spins displaced by \mathbf{c} are anti-parallel. As will be discussed in Sec. IV A, the single ion magnetic anisotropy in SrHo_2O_4 allows an unambiguous association of red sites with $\mathbf{q}_{\mathbf{c}} = 0$ correlations while spins on blue sites host $\mathbf{q}_{\mathbf{c}} \sim 0.5\mathbf{c}^*$ type correlations. For clarity this assignment will be employed from this point though it will not be justified until Sec. IV A. The correlation lengths along \mathbf{c} can be estimated by $2/(\text{FWHM}_{\text{expt}}^2 - \text{FWHM}_{\text{reso}}^2)^{-\frac{1}{2}}$, where $\text{FWHM}_{\text{expt}}$, $\text{FWHM}_{\text{reso}}$ are experimental and instrumental full width at half maximum. At $T = 1.5$ K we find the correlation lengths along \mathbf{c} are indistinguishable at $13.3(3)\text{\AA}$ and $13.6(3)\text{\AA}$ for red and blue ladders respectively.

The evolution of these two kinds of short range correlations across T_{N} were probed by single crystal ENS in the $(0KL)$ and (HOL) planes down to $T \sim 0.3$ K. Firstly L -

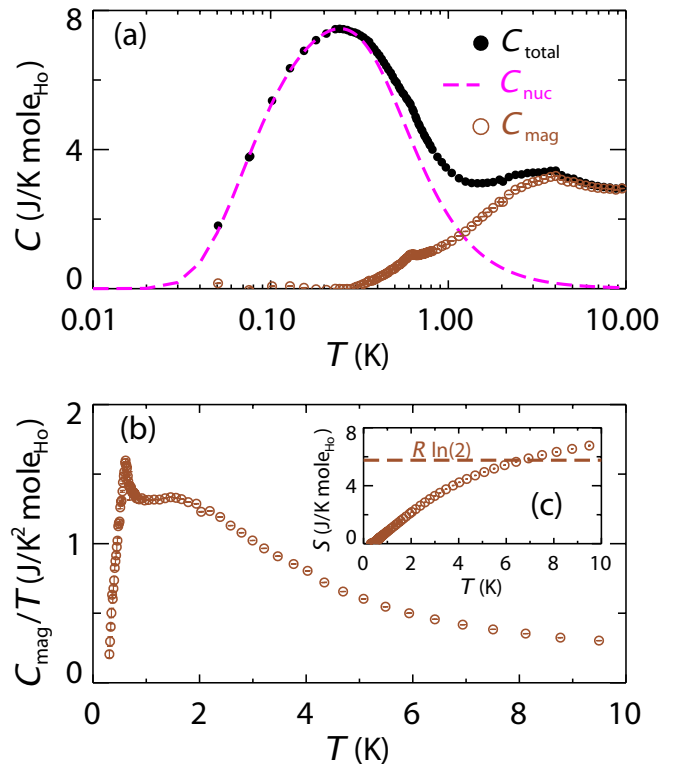


FIG. 3. (a) Specific heat of SrHo_2O_4 as a function of T . Filled symbols show the experimental total specific heat; the magenta long dashed line shows the calculated specific heat due to a nuclear Schottky anomaly; open symbols show the magnetic specific heat obtained by subtracting the nuclear Schottky anomaly from the total specific heat. (b) Magnetic specific heat over T versus T . (c) shows the entropy versus T . The dashed line shows the entropy of an Ising doublet.

scans at all accessible (n_a, n_b, n_c) and $(n_a, n_b, n_c + 1/2)$ magnetic peaks (n_a, n_b, n_c being integers) are resolution limited at $T = 0.28$ K. This is evidence of quasi-1D correlations over length scales exceeding $286(5)\text{\AA}$ and $100(1)\text{\AA}$ respectively for red and blue ladders. These lower bounds were obtained from L -scans at (030) and $(00\frac{1}{2})$ respectively. The different limits arise because the L -scan is a rocking scan for red ladders but a longitudinal scan for blue ladders, which results in better resolution for red ladders.

Temperature dependent $(0K0)$ scans for $K \in [0.5, 4.5]$ between 0.28 K and 10 K were acquired to probe correlations between red chains with relative displacement along \mathbf{b} [Fig. 5(a)]. Upon cooling, a broad intensity modulation develops and turns into resolution limited Bragg peaks for T below $T_{\text{N}} = 0.68(2)$ K. Measurements at (200) and (030) indicate the correlation length for red spins exceeds $57(1)\text{\AA}$ and $64(1)\text{\AA}$ respectively along \mathbf{a} and \mathbf{b} at $T = 0.28$ K.

Despite a spin correlation length exceeding $100(1)\text{\AA}$ along \mathbf{c} , blue chains however, fail to develop conventional long range inter-chain correlations [Fig. 5(b)(c)]. While these inter-chain correlations are enhanced at low

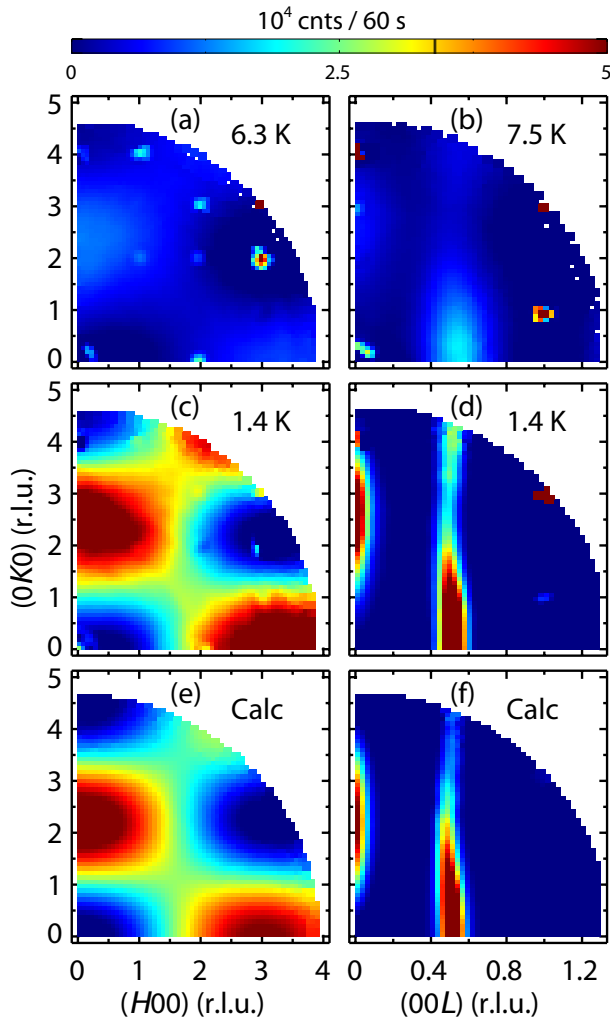


FIG. 4. T -dependent elastic magnetic neutron scattering indicating quasi-one-dimensional short range order in SrHo_2O_4 . (a)(c) show measurements in the $(HK0)$ reciprocal lattice plane while (b)(d) are from the $(0KL)$ plane. Measurements at 50 K were subtracted to eliminate nuclear scattering. (e) and (f) show $J_1 - J_2$ model calculations at 1.4 K with exchange constants determined from Fig. 2.

T as manifested by sharpening of the peaks, the peak width remains much broader than the instrumental resolution shown by horizontal bars. A detailed view of H - and K -scans through $(00\frac{1}{2})$ at $T = 0.28$ K is provided in Fig. 6. The broad modulations are well described by Lorentzian fits that correspond to correlation length along \mathbf{a} and \mathbf{b} of just $6.0(1)$ Å and $17.5(3)$ Å respectively. The H -scan however, also includes a curious small sharp component that indicates some correlations between blue chains persists to a separation of $165(9)$ Å perpendicular to their easy axis. This observation merits further theoretical and experimental exploration.

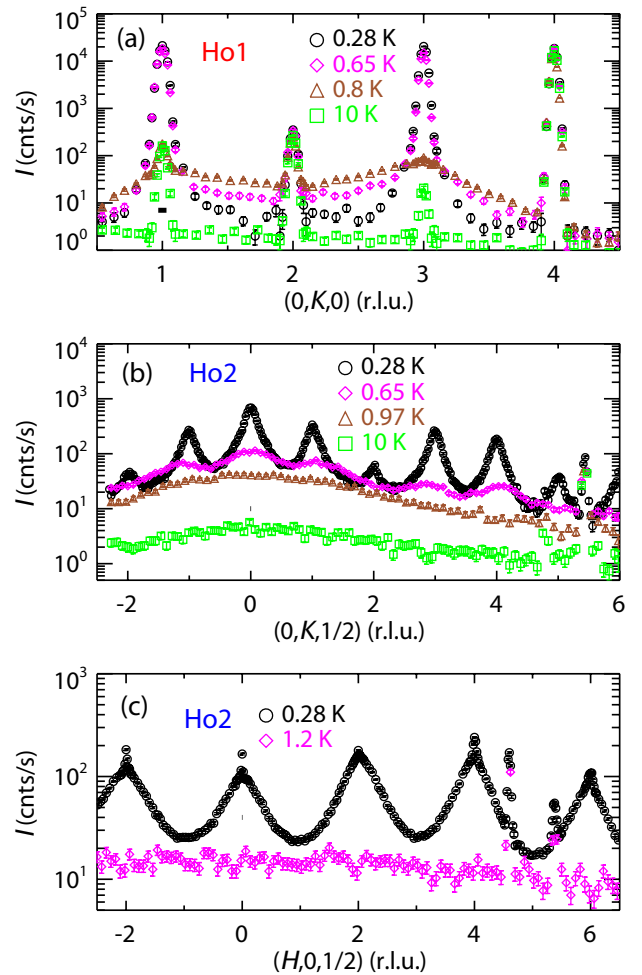


FIG. 5. Thermal evolution of inter-chain correlations for red and blue sites probed by neutrons. (a) shows $(0, K, 0)$ scans probing the correlations along \mathbf{b} between red chains at several temperatures. (b) and (c) respectively show $(0, K, \frac{1}{2})$ and $(H, 0, \frac{1}{2})$ scans that probe correlations along \mathbf{b} and \mathbf{a} for blue chains. Horizontal bars represent instrumental resolution. Sharp peaks at $K \sim 5.5$ in (b), at $H \sim 4.6$ and $H \sim 5.4$ in (c) are the results of Bragg scattering from the copper sample mount.

IV. ANALYSIS

A. Single ion anisotropy

As has been suggested in previous sections, magnetic anisotropy plays an all important role in the magnetic properties of SrHo_2O_4 . In the anisotropic environment of the solid, the $J = 8$ multiplet of Ho^{3+} is split into multiple levels resulting in the anisotropic susceptibility²⁰ shown in Fig. 2. The C_s point group symmetry of both red and blue Ho^{3+} sites implies an easy magnetic axis either along \mathbf{c} or within the \mathbf{ab} plane. A CEF calculation based on the point charge approximation²², where CEF at Ho site is approximated by the static electric field from 6 surrounding O^{2-} ions, shows both red and blue sites

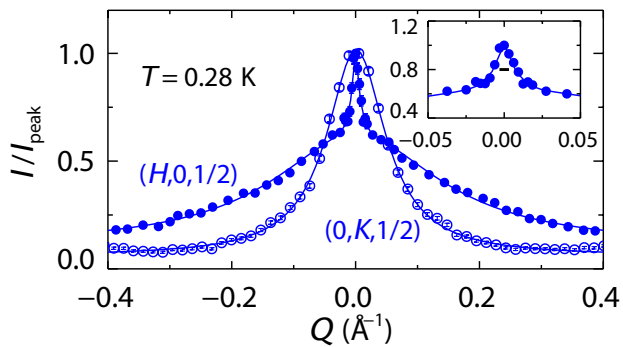


FIG. 6. Inter-chain correlations for blue sites in SrHo_2O_4 probed by neutrons. Filled and empty circles are from H - and K -scans at $(00\frac{1}{2})$ measured at 0.28 K. The solid lines show fits to the data. Insert shows a sharp component of H -scan in detail, the horizontal bar is the instrumental resolution. Data from different sample orientations are normalized to the peak count rate.

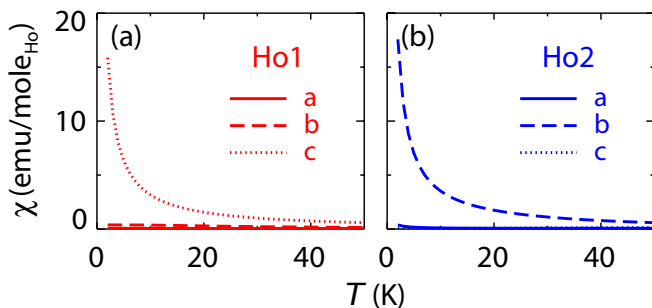


FIG. 7. Calculated single ion magnetic susceptibility for (a) red Ho1 site and (b) blue Ho2 site in SrHo_2O_4 along three axes based on CEF level schemes calculated according to point charge approximation.

have a doublet ground state. The single ion magnetic susceptibility calculated based on the point charge CEF level schemes (Fig. 7) reveals the Ising doublet ground state for red Ho1 (blue Ho2) sites have an easy axis along \mathbf{c} (b). We infer the temperature dependent susceptibility (Fig. 2) for fields along \mathbf{c} and \mathbf{b} are due to red and blue sites respectively. For blue sites a finite moment along \mathbf{a} is allowed by symmetry, however, since χ_a is minimal it will be neglected.

With this information about the magnetic anisotropy for the two Ho sites, it can be inferred that the scattering in the $(HK0)$ plane in Fig. 4(a)(c) is due to red ladders because there is no decrease in intensity for $\mathbf{q} \parallel (0K0)$ which would be the case for easy \mathbf{b} -axis blue sites. This is a consequence of the polarization factor in magnetic neutron scattering which ensures that neutrons only probe magnetic moments perpendicular to \mathbf{q} .²³ An analogous polarization argument shows that the scattering in $(0KL)$ plane with $\mathbf{q}_c \sim 0.5\mathbf{c}^*$ arises from blue sites.

TABLE I. Magnitude of dipolar interaction energies between neighboring spins in SrHo_2O_4 assuming Ising moment size of $6.2 \mu_B$ and $9.9 \mu_B$ on red and blue sites respectively. The numbering of Ho^{3+} ions is as shown in Fig. 1(b). Intra-ladder dipolar energies (row 1-4) are positive/negative for FM/AFM interactions. For comparison, the corresponding ANNNI model exchange constants inferred from susceptibility fits are in the third column.

Pair of Spins	Dipolar Energy (meV)	J_{ANNNI} (meV)
Ho1(1) - Ho1(3)	-0.01	J_{r1} -0.10(2)
Ho1(1) - Ho1(1)+ \mathbf{c}	0.10	J_{r2} 0.04(3)
Ho2(1) - Ho2(3)	0.08	J_{b1} -0.14(3)
Ho2(1) - Ho2(1)+ \mathbf{c}	-0.13	J_{b2} -0.21(1)
Ho1(1) - Ho2(3)	0.05	
Ho1(4) - Ho2(1)	0.00	

B. ANNNI model

The dominant intra-ladder SRO (Fig. 4) suggests the minimal model for SrHo_2O_4 is a collection of two types of independent Ising zig-zag spin ladders with different inter-leg interactions J_{r1}, J_{b1} and intra-leg interactions J_{r2}, J_{b2} for the red and blue chains respectively [Fig. 1(b)]. The underlying model for both chains is the exactly solvable 1D ANNNI model⁷:

$$H = \sum_i -J_1 S_i S_{i+1} - J_2 S_i S_{i+2}, \quad (1)$$

where $S_i = \pm 1$. Dipolar interactions between spins in SrHo_2O_4 can be comparable to T_N because of the large magnetic moment size for Ho^{3+} ions. To be specific, consider magnetic moment size of $6.2 \mu_B$ and $9.9 \mu_B$ oriented along the easy axes of red and blue Ho^{3+} sites respectively. These are the magnetic moment sizes for the two Ho sites estimated in this study that will be justified in detail in Sec. IV C. The corresponding dipolar interaction energies between neighboring Ho^{3+} ions are listed in Table. I. These energies are found to be of order a Kelvin and extend with considerable strength to further neighbors. The ANNNI model should thus be considered as a minimal effective model to describe each of the spin ladders in SrHo_2O_4 . Antisymmetric Dzyaloshinskii-Moriya (DM) interactions are also allowed in the low crystalline symmetry of SrHo_2O_4 . The strong Ising anisotropy however, extinguishes intra-ladder DM interactions because all spins within each type of ladder are oriented along the same easy axis. While DM interactions between red and blue ladders are allowed, the different modulation wave vectors for the two types of ladders (0 and $0.5\mathbf{c}^*$ respectively) render these and all other inter-ladder interactions ineffective at the mean field level. This may explain why the simple model of independent ANNNI chains that we shall explore in the following provides a good basis for describing the magnetism of SrHo_2O_4 outside of the critical regime near T_N .

To determine the exchange constants J_1 and J_2 we fit the anisotropic susceptibility to the analytical result for

the susceptibility of the ANNNI model. The exchange constants for red and blue chains are denoted by $J_{r1,2}$ and $J_{b1,2}$ respectively. The uniform magnetic susceptibility χ can be related to the two point correlation function as follows

$$\chi \equiv \lim_{h \rightarrow 0} \frac{\partial \langle M \sum_i S_i \rangle}{\partial h} = NM^2 \beta \tilde{G}(\mathbf{q} = 0), \quad (2)$$

where N is the number of sites in the spin chain, M is the dipole moment of each spin, h is the magnetic field, $\beta = 1/k_B T$, $\tilde{G}(\mathbf{q} = 0) = \sum_i G(i)$, and $G(i) \equiv \langle S_0 S_i \rangle$ is the two-point correlation function for the 1D ANNNI model. The fits were restricted to data points with $T \leq 20$ K where the influence from higher CEF levels can be neglected.

For red chains (accessible through χ_c), the best fit is achieved for $J_{r1} = -0.10(2)$ meV and $J_{r2} = 0.04(3)$ meV. The corresponding calculated susceptibility is shown as a red dashed line in Fig. 2. These exchange parameters define an unfrustrated ANNNI chain where all interactions are simultaneously satisfied by the Néel structure ($\uparrow\downarrow\uparrow\downarrow$). χ_b for blue chains is best fit with $J_{b1} = -0.14(3)$ meV and $J_{b2} = -0.21(1)$ meV. While these competing interactions produce incommensurate short range correlations at finite temperatures, the ground state is the double Néel structure ($\uparrow\uparrow\downarrow\downarrow$).⁷ The magnetic moment sizes extracted from fitting the susceptibility data for red and blue sites are $5.5(3) \mu_B$ and $8.1(2) \mu_B$ respectively, which are consistent with neutron diffraction measurements.^{11,13} These effective Ising exchange constants are compared to the dipolar interaction strengths in Table I. The significant discrepancies might be accounted for by contributions to the effective ANNNI interactions from superexchange, longer range dipole interactions, as well as higher order effects from inter-ladder interactions.

A critical test of the quasi-1D ANNNI model for SrHo_2O_4 is offered by Fig. 4. Frames (e) and (f) show a calculation of the diffuse magnetic neutron scattering intensity at the given temperature from such spin chains based on the Fourier transformation of the two-point correlation function $G(r)$ for the exchange constants derived from χ_c and χ_b and the particular crystalline structure of the ladders. Only an overall scale factor and a constant background were varied to achieve the excellent account of the ENS data in Fig. 4(c)-(d). Though no correlations between spin chains are included, the finite width of the zig-zag spin ladders and the two different red ladder orientations in SrHo_2O_4 [Fig. 1(b)] produce the checkerboard-like structure in the $(HK0)$ plane. It is remarkable that a purely 1D model can account for the magnetism of a dense 3D assembly of spin chains. Contributing to this are surely the different spin orientations for red and blue sites and the incompatible modulation wave vectors.

C. Low temperature magnetic structure

While the strictly 1D ANNNI model can only form LRO at $T = 0$ K, finite inter-chain interactions can in-

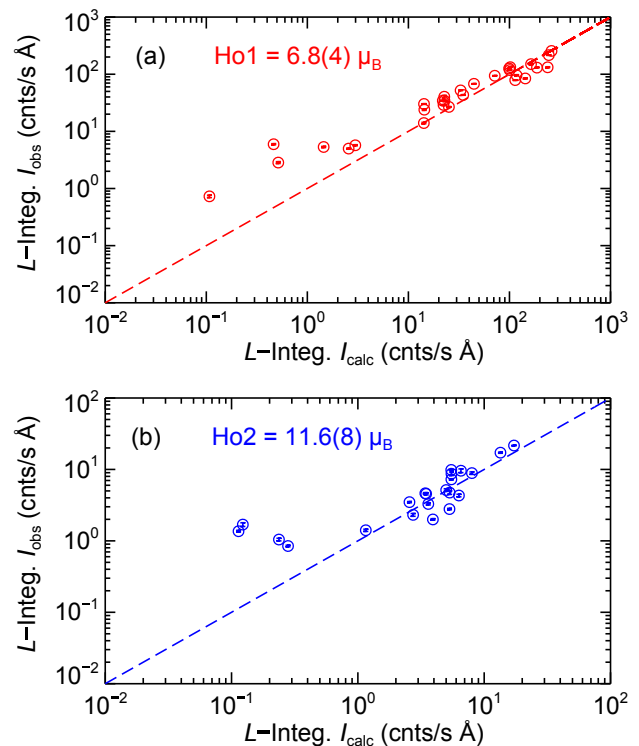


FIG. 8. Magnetic structure refinement for SrHo_2O_4 based on L -integrated peak intensities measured for $T = 0.3$ K. (a) and (b) show the refinement results for red and blue sites respectively. Long dashed lines represent the $y = x$ line.

duce LRO at finite T_N . ENS (Fig. 5) reveal that the red sites form 3D LRO while the blue sites develop long range correlations only along the chain direction. To characterize the corresponding magnetic structures and to estimate the static magnetic moment sizes, a magnetic structure refinement was carried out based on ENS measured for $T = 0.3$ K.

We first consider the 3D ordered red sites. Since the propagation vector $\mathbf{q}_c = 0$, magnetic Bragg scattering overlaps with nuclear Bragg peaks. For unpolarized neutrons employed in this study, the total Bragg scattering intensity is simply the sum of these two contributions.

Representation analysis²⁴ shows that for $\mathbf{q}_c = 0$ there are two magnetic structures that are compatible with both the easy \mathbf{c} -axis anisotropy and the short range magnetic order inferred from the diffuse neutron scattering pattern (Fig. 4). Using the labeling of red Ho1 atoms in the unit cell as shown in Fig. 1(b), these two structures can be represented as $\phi_{1,2} \equiv (\mathbf{m}_1, \mathbf{m}_2, \mathbf{m}_3, \mathbf{m}_4) = m\hat{\mathbf{c}}(1, \pm 1, -1, \mp 1)$, where \mathbf{m}_i is the magnetic moment on atom i , m is the moment size, and $\hat{\mathbf{c}}$ is a unit vector along \mathbf{c} -axis. The experimental observation that all nuclear forbidden Bragg peaks in the $(H0L)$ plane with even H indices have negligible magnetic scattering intensity shows that ϕ_1 is the appropriate magnetic structure, since ϕ_2 would give rise to magnetic Bragg peaks at such locations.

To extract the magnetic moment size for Ho1, the L -integrated intensities for all accessible Bragg peaks with integer indices, which contain both nuclear and magnetic scattering contributions, were compared to the calculated neutron diffraction intensity for the ϕ_1 structure. The nuclear structure factors were calculated according to the crystal structure determined in a previous study.⁸ Measurements in the $(0KL)$ and $(H0L)$ planes were co-refined while keeping the ratio of scale factors in the two reciprocal lattice planes fixed at the mass ratio for the samples employed in each reciprocal lattice plane. The best fit shown in Fig. 8(a) yields a moment size of $6.8(4) \mu_B$ for the red Ho1 sites. The correspondence with the red chain moment of $5.5(3) \mu_B$ derived from ANNNI fits to χ_c corroborates the assumptions that underlie this analysis.

For the blue sites, where the correlation length is short along \mathbf{a} and \mathbf{b} directions, we approximate the peak shape as the product of a sharp Gaussian along \mathbf{c} with two broad Lorentzians along \mathbf{a} and \mathbf{b} . For measurements in the $(0KL)$ plane, the peak width of the Gaussian and the in-plane Lorentzian were obtained by fitting the experimental data, while the peak width for the out of plane Lorentzian was assumed to be identical at all peak positions and was approximated by the average peak width along \mathbf{a} measured in the $(H0L)$ plane. Note that when taking the average, each peak width was weighted by the corresponding integrated intensity so that stronger peaks contribute with larger weight to the average: $\overline{\text{FWHM}} = \sum_i \text{FWHM}_i \cdot I_i / \sum_i I_i$. Following the same procedure, the out of plane Lorentzian width for peaks within the $(H0L)$ plane were obtained from measurements in the $(0KL)$ plane.

Representation analysis for $\mathbf{q}_c = 0.5\mathbf{c}^*$ allows spin structures of the form $\psi = m_1 \hat{\mathbf{b}}(1, 1, 0, 0) + m_2 \hat{\mathbf{b}}(0, 0, 1, 1)$. Since there is no 3D long range order, this magnetic structure only reflects the locally ordered pattern. It is assumed that $|m_1| = |m_2|$ since all four Ho2 ions in the unit cell are equivalent in the paramagnetic phase and no significant improvement in refinement was obtained by allowing m_1 and m_2 to vary independently. With this constraint there are still two different magnetic structures $\psi_{1,2} = m \hat{\mathbf{b}}(1, 1, \pm 1, \pm 1)$, which can be regarded as two domain types that are related by mirror reflection about the \mathbf{ab} plane. With no *a priori* reason to favor one domain over the other, it is assumed that both domains contribute equally. Using the same scale factor obtained from refinement of the red Ho1 moment size, least squares fit to the L -integrated intensities of all accessible peaks of the form $(0K \frac{2n+1}{2})$ and $(H0 \frac{2n+1}{2})$ was conducted. This resulted in a moment size of $11.6(8) \mu_B$ for blue Ho2. Fig. 8(b) provides a comparison of the measured and calculated integrated intensities.

The analysis of anisotropic diffuse scattering that is the basis for the moment sizes extracted for blue sites is subject to systematic uncertainties that are not reflected in the error bars. We therefore consider the magnetic moment sizes extracted from the neutron measurements

[$6.8(4) \mu_B$ and $11.6(8) \mu_B$ for red and blue Ho] consistent with those obtained from the ANNNI susceptibility fits [$5.5(3) \mu_B$ and $8.1(2) \mu_B$ respectively]. Combining these results, which are subject to different systematic errors leads to an experimental average result of $6.2(3) \mu_B$ and $9.9(4) \mu_B$ for red and blue sites respectively. The difference in the moment sizes for red and blue sites indicates the different CEF environment for these two sites. The moment on blue sites is close to the maximal magnetic moment size of $10 \mu_B$ for a Ho^{3+} ion, which indicates a strong Ising character for blue Ho2 ions.

D. Temperature dependent spin correlations

To probe the interplay between the two types of spin ladders, scans for a range of T were carried out through the (030) and $(00\frac{1}{2})$ peaks. These peaks respectively arise from red and blue chains (Fig. 9). The result for red sites is shown in Fig. 9(a) and (b). The integrated intensity of the peak, a measure of the staggered magnetization squared, grows below T_N then saturates at $T_S = 0.52(2)$ K. This is consistent with a second order phase transition in a uniaxial spin system where the gap in the magnetic excitation spectrum produces a characteristic saturation temperature. Near T_N , the critical exponent $\beta = 0.36(2)$ is consistent with that for the 3D Ising model [$\beta_{3DI} = 0.3258(14)$], but also indistinguishable from the 3D XY [$\beta_{3DXY} = 0.3470(14)$] and 3D Heisenberg models [$\beta_{3DH} = 0.3662(25)$].²⁵ The peak width [Fig. 9(b)] decreases markedly upon cooling towards T_N signalling the development of commensurate long range correlations among red spins.

A rather different situation is found for the blue chains. There is no anomaly in the temperature dependent L -integrated intensity of the $(00\frac{1}{2})$ peak at T_N but a gradual increase upon cooling that terminates at T_S [Fig. 9(c)]. The nature of spin correlations along the blue chains is probed by the position and width of the $(00\frac{1}{2})$ peak. Both evolve continuously across T_N in semi-quantitative agreement with the ANNNI model, using the parameters that also describe the susceptibility and diffuse neutron scattering data. The trend however, ceases at T_S with a peak center position of $0.501\mathbf{c}^*$. The deviation, Δq_c , from the commensurate position $0.5\mathbf{c}^*$ is significant and a long wave length modulated structure is apparent as an oscillation of the centers for other $(0K\frac{1}{2})$ type peaks with $K = 1, 2, 3, 4, 5$ [inset to Fig. 9(d)]. This is consistent with $G(r)$ for the incommensurate zig-zag ladder, which is indicated by the dashed line in the inset.

V. DISCUSSION AND CONCLUSION

To understand the very different behaviors of red and blue spin chains we consider the ground state degeneracies and the corresponding domain wall structures of these two weakly coupled spin systems (Fig. 10). For

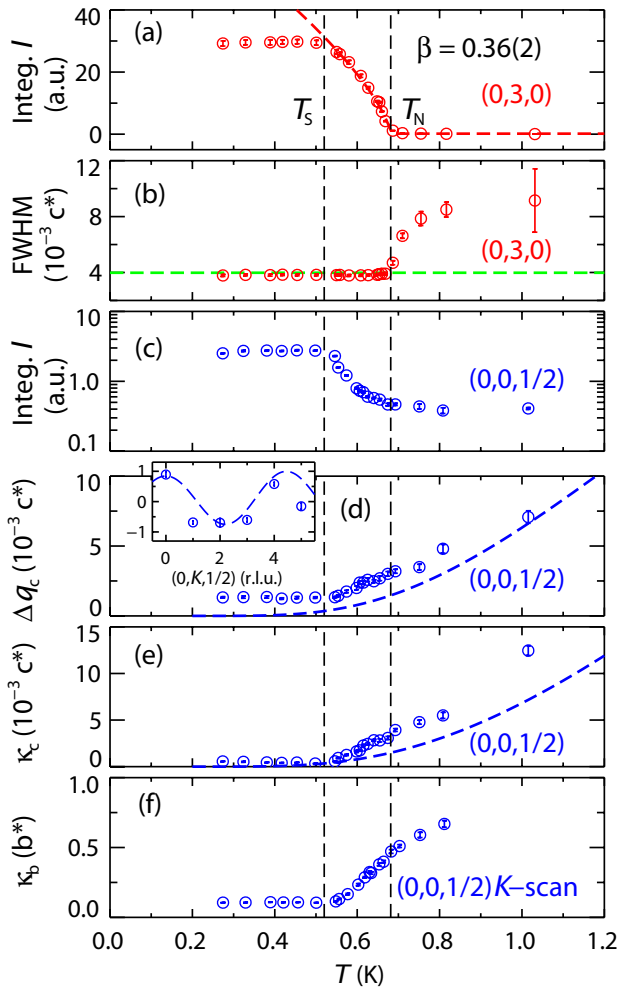


FIG. 9. Spin correlations versus T in SrHo_2O_4 probed by neutrons. (a)-(e) show results from L -scans at (030) (red) and $(00\frac{1}{2})$ (blue) that probe correlations along red and blue chains respectively. (a) and (b) show integrated intensities and peak widths for (030) . The green dashed line in (b) shows the instrumental resolution. (c) shows integrated intensities for $(00\frac{1}{2})$. (d) shows the peak shift from $(00\frac{1}{2})$. The inset shows the peak shift along c^* from $(0K\frac{1}{2})$. The dashed line shows the predicted shift based on the $J_1 - J_2$ model. (e) shows the inverse correlation length κ_c derived as the half width at half maximum of resolution convoluted Lorentzian fits. (f) shows κ_b extracted from K -scans at $(00\frac{1}{2})$. Black dashed lines indicate T_N and T_S . Blue dashed lines in (d) and (e) are ANNNI model calculations based only on the exchange constants obtained from the data in Fig. 2.

the red chains there are two ground states which are time-reversal partners. These are shown as $R1$ and $R1^*$ in Fig. 10(a). A transition between these structures involves a domain wall that costs a finite energy of $\Delta E = -2J_{r1} + 4J_{r2}$. The situation is more complicated in the blue chains. In their ground state there are four sites per magnetic unit cell and therefore four different types of domains that correspond to shifting the $(\uparrow\uparrow\downarrow\downarrow)$ motif with respect to the origin. We label these as

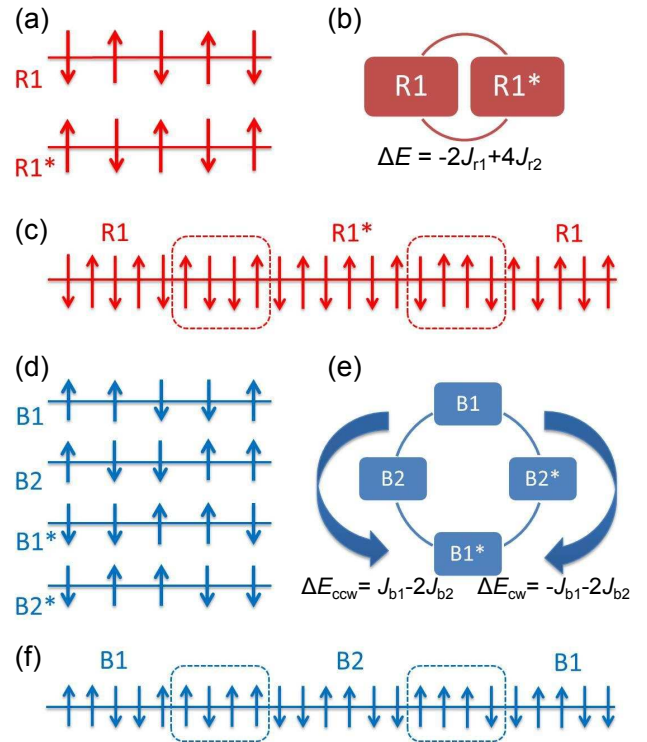


FIG. 10. Ground state degeneracy and domain walls of ANNNI chains in SrHo_2O_4 . (a) and (b) show the two fold degenerate ground states for red chains and the corresponding domain wall. (c) illustrates that a $R1$ to $R1^*$ domain wall is identical to a $R1^*$ to $R1$ domain wall (up to time reversal). (d) and (e) show the more complicated situation for blue chains where the ground state is four fold degenerate and the domain walls are chiral. (f) illustrates the chiral character of the domain walls in blue chains: a $B1$ to $B2$ domain wall is different from a $B2$ to $B1$ domain wall. Refer to Sec. V for a detailed description. Dashed rectangles in (c) and (f) encircle spins whose bond energies are affected by transition to a different ground state, and thus represent the domain walls.

$B1$, $B2$ and their time-reversal partners $B1^*$ and $B2^*$ in Fig. 10(d). Low energy domain walls correspond to transitions between ground states that are shifted by only one lattice site. Their “chiral” character can be appreciated by comparing the energy cost of a domain wall that goes from $B1$ to $B2$ [counterclockwise in Fig. 10(e)] to a domain wall that effectuates a transition from $B2$ to $B1$ [clockwise in Fig. 10(e)]. By convention we choose the right direction as the positive direction of the spin chain. The domain walls are chiral because their energy depends on handedness in Fig. 10(e): $\Delta E_{ccw} = J_{b1} - 2J_{b2}$ and $\Delta E_{cw} = -J_{b1} - 2J_{b2}$. The larger ground state degeneracy and the correspondingly more complex domain wall structures for blue chains complicates their attainment of thermodynamic equilibrium.

It is useful to consult the 3D ANNNI model⁷ to understand how the different domain wall structures may affect the low temperature magnetic ordering. For $J_{r2}/J_{r1} = -0.4(3)$, the mean field phase diagram of the 3D ANNNI

model features a single phase transition from a paramagnetic (PM) phase to 3D Néel order, as we observe for the red chains in SrHo₂O₄. The exchange parameters of the blue chains [$J_{b2}/J_{b1} = 1.5(3)$] however, place these in a complicated part of the 3D ANNNI phase diagram. Between the PM phase and 3D double-Néel order exists a large number of 3D LRO phases with different modulation wave vectors. These can be described in terms of different arrangements of domain wall defects within the double Néel structure. Effective interactions between defects stabilize these various phases at different temperatures.

With this picture in mind, the continuous peak center shift observed in Fig. 9(d) reflects domain wall rearrangement along blue chains. Focusing on domain walls, full 3D LRO requires registry in the placement of transitions between domains along all blue spin chains. Such collective domain wall motion requires rearrangement of large numbers of spins and so can be a slow process. Further, in the non-Kramers doublet ground state of Ho³⁺, a spin flip can only take place through tunneling or a thermal process involving higher CEF levels. In the recently proposed CEF level scheme¹³ blue sites have a large energy gap (~ 12 meV) to the first excited state (compared to ~ 1 meV for red sites). This can be expected to reduce the tunneling and thermal rate for blue spin flips at low temperatures.

We now return to the important experimental observation that the spin configuration on blue chains ceases to evolve when red chains become fully ordered for $T < T_S$ (Fig. 9). This indicates fluctuating exchange fields from spin dynamics in the red chains - which have a lower

barrier to spin flips - are the dominant source of spin dynamics on blue chains. Ironically, it thus appears to be the development of saturated order on red chains that increases the relaxation time for domain wall motion in blue chains and stunts their inter-chain correlations.

In conclusion, our experiments on SrHo₂O₄ suggest a magnetically disordered state can persist in the low T limit within a high quality crystal not because it is energetically favorable but because it is the thermodynamic equilibrium state when, upon cooling, ergodicity is lost. SrHo₂O₄ also illustrates the remarkably disruptive impact of topological defects in d dimensions (here $d = 1$) on $d + 1$ dimensional order. Combining the ingredients of large scale emergent structures from frustration and reduced dimensionality, kinetically trapped spin disorder may actually be possible without quenched disorder.

ACKNOWLEDGMENTS

We thank O. Tchernyshyov, J. Zang, Y. Wan for discussion. Work at IQM was supported by the US Department of Energy, office of Basic Energy Sciences, Division of Materials Sciences and Engineering under grant DE-FG02-08ER46544. This work utilized facilities supported in part by the US National Science Foundation under Agreement No. DMR-0944772. Research conducted at ORNL's High Flux Isotope Reactor was sponsored by the Scientific User Facilities Division, Office of Basic Energy Sciences, US Department of Energy. Ames Laboratory is operated for the U.S. Department of Energy by Iowa State University under Contract No. DE-AC02-07CH11358.

* Present address: Department of Applied Physics, Stanford University, Stanford, CA 94305

¹ S.-H. Lee, C. Broholm, G. Aeppli, A. P. Ramirez, T. G. Perring, C. J. Carlile, M. Adams, T. J. L. Jones, and B. Hessen, EPL (Europhysics Letters) **35**, 127 (1996).

² I. A. Zaliznyak, C. Broholm, M. Kibune, M. Nohara, and H. Takagi, Phys. Rev. Lett. **83**, 5370 (1999).

³ I. S. Hagemann, Q. Huang, X. P. A. Gao, A. P. Ramirez, and R. J. Cava, Phys. Rev. Lett. **86**, 894 (2001).

⁴ S. Nakatsuji, Y. Nambu, H. Tonomura, O. Sakai, S. Jonas, C. Broholm, H. Tsunetsugu, Y. Qiu, and Y. Maeno, Science **309**, 1697 (2005).

⁵ Y. Okamoto, H. Yoshida, and Z. Hiroi, Journal of the Physical Society of Japan **78**, 033701 (2009).

⁶ I. Klich, S. H. Lee, and K. Iida, Nature Communications **5** (2014), 10.1038/ncomms4497.

⁷ W. Selke, Physics Reports **170**, 213 (1988), and references therein.

⁸ H. Karunadasa, Q. Huang, B. G. Ueland, J. W. Lynn, P. Schiffer, K. A. Regan, and R. J. Cava, Phys. Rev. B **71**, 144414 (2005).

⁹ S. Ghosh, H. D. Zhou, L. Balicas, S. Hill, J. S. Gardner, Y. Qiu, and C. R. Wiebe, Journal of Physics: Condensed

Matter **23**, 164203 (2011).

¹⁰ T. J. Hayes, O. Young, G. Balakrishnan, and O. A. Petrenko, Journal of the Physical Society of Japan **81**, 024708 (2012).

¹¹ O. Young, L. C. Chapon, and O. A. Petrenko, Journal of Physics: Conference Series **391**, 012081 (2012).

¹² O. Young, A. R. Wildes, P. Manuel, B. Ouladdiaf, D. D. Khalyavin, G. Balakrishnan, and O. A. Petrenko, Phys. Rev. B **88**, 024411 (2013).

¹³ A. Fennell, V. Y. Pomjakushin, A. Uldry, B. Delley, B. Prévost, A. Désilets-Benoit, A. D. Bianchi, R. I. Bewley, B. R. Hansen, T. Klimczuk, R. J. Cava, and M. Kenzelmann, Phys. Rev. B **89**, 224511 (2014).

¹⁴ O. A. Petrenko, G. Balakrishnan, N. R. Wilson, S. de Brion, E. Suard, and L. C. Chapon, Phys. Rev. B **78**, 184410 (2008).

¹⁵ T. J. Hayes, G. Balakrishnan, P. P. Deen, P. Manuel, L. C. Chapon, and O. A. Petrenko, Phys. Rev. B **84**, 174435 (2011).

¹⁶ D. L. Quintero-Castro, B. Lake, M. Reehuis, A. Niazi, H. Ryll, A. T. M. N. Islam, T. Fennell, S. A. J. Kimber, B. Klemke, J. Ollivier, V. G. Sakai, P. P. Deen, and H. Mutka, Phys. Rev. B **86**, 064203 (2012).

- ¹⁷ O. A. Petrenko, *Low Temperature Physics* **40**, 106 (2014).
- ¹⁸ H. Li, C. Zhang, A. Senyshyn, A. Wildes, K. Schmalzl, W. Schmidt, M. Boehm, E. Ressouche, B. Hou, P. Meuffels, G. Roth, and T. Brückel, *Frontiers in Physics* **2** (2014), 10.3389/fphy.2014.00042.
- ¹⁹ J. A. Rodriguez, D. M. Adler, P. C. Brand, C. Broholm, J. C. Cook, C. Brocker, R. Hammond, Z. Huang, P. Hundertmark, J. W. Lynn, N. C. Maliszewskyj, J. Moyer, J. Orndorff, D. Pierce, T. D. Pike, G. Scharfstein, S. A. Smee, and R. Vilaseca, *Measurement Science and Technology* **19**, 034023 (2008).
- ²⁰ J. Jensen and A. Mackintosh, *Rare earth magnetism: structures and excitations*, International series of monographs on physics (Clarendon Press, 1991).
- ²¹ A. Tari, *The Specific Heat of Matter at Low Temperatures* (Imperial College Press, 2003).
- ²² M. Hutchings, *Solid State Physics* **16**, 227 (1964).
- ²³ G. Squires, *Introduction to the Theory of Thermal Neutron Scattering* (Cambridge University Press, 2012).
- ²⁴ A. Wills, *Physica B: Condensed Matter* **276C278**, 680 (2000).
- ²⁵ H. Kleinert, *Phys. Rev. D* **60**, 085001 (1999).